sustainability

MDPI

Article

An improved method for disassembly depth optimization of end-of-life smartphones based on PSO-BP neural network predictive model

Shengqiang Jiao, Lin Li *, Fengfu Yin, Yang Yu

College of Electromechanical Engineering, Qingdao University of Science and Technology, Qingdao 266061, China

* Correspondence: ll@qust.edu.cn; Tel.: +86-17561737080

Abstract

Disassembly is a crucial step in the remanufacturing of end-of-life (EoL) electronic products. For disassembly depth optimization of EoL electronic products, a feasibility model with fast convergence and low mean squared error (MSE) is needed to improve optimization accuracy. However, with the use of backpropagation neural network (BPNN) model or mathematical model often results in slow convergence and high MSE due to the randomness of initial weights and biases. In this study, an improved method for disassembly depth optimization of smartphones based on Particle Swarm Optimization-BPNN (PSO-BPNN) predictive model is proposed. Compared with traditional BPNN optimization method, the proposed method in this study is that the BPNN predictive model is optimized by using PSO, which shows superior predictive performance and reduces the MSE. The case of the 'Huawei P7' is used to verify the feasibility of the proposed method. The results show that the proposed method maintains disassembly profit while reducing disassembly time and carbon emissions by 17.1% and 7.8% respectively. Compared with BPNN model, PSO-BPNN model converges 18.6%, 32.8%, and 16.6% faster in predicting disassembly time, profit and carbon emissions, respectively, with MSE reduction of 92.95%, 96.51%, and 92.74%, respectively.

Keywords: Disassembly depth optimization; EoL smartphones; PSO-BPNN; MSE; Pareto solutions

Academic Editor: Firstname Lastname

Received: date
Revised: date
Accepted: date
Published: date

Citation: To be added by editorial staff during production.

Copyright: © 2025 by the authors. Submitted for possible open access publication under the terms and conditions of the Creative Commons Attribution (CC BY) license (https://creativecommons.org/licenses/by/4.0/).

1. Introduction

Nowadays, the rapid development of science and technology has accelerated product updates, which results in the generation of many EoL products [1]. Waste electrical and electronic equipment (WEEE) is one of the fastest-growing waste streams globally, with EoL smartphones accounting for a significant proportion [2]. As an example of China, about 30 million EoL smartphones are generated annually, but the recycling rate even less than 1%, with most being discarded or incinerated [3,4]. With the increasing amount of WEEE, EoL smartphones are an important component that cannot be ignored due to their variety and high recycling value [5]. In order to recycle resources and protect the environment, many countries have carried out stricter legislation and paid more attention to the recycling and remanufacturing of EoL products, such as the "Product Recycling Law" in Europe and the "Recyclability Law" in Japan [6,7].

As a crucial step in the recycling process of EoL products, disassembly has an irreplaceable role in sustainable development [8]. Compared to complete disassembly, the partial disassembly is more practical and has been widely adopted, becoming the mainstream choice for many disassembly enterprises [9,10]. Yin et al. [11] proposed a partial sequence-dependent disassembly line balancing problem considering tool requirements. To avoid unnecessary work and labor waste, Yin et al. [12] proposed a multimanned partial disassembly line balancing problem. To determine the optimal disassembly depth in improving efficiency and reducing costs has always been a concern for enterprises and researchers [13]. Wu et al. [14] solved the EoL Li-ion recycling problem by extending the disassembly depth of Li-ion batteries. Gao et al. [15] constructed a partially observable multi-intelligence reinforcement learning environment that combines the structure of an electric vehicle battery with a disassembly task for disassembly depth optimization. Hu et al. [16] proposed a generic ontology model and combined it with a rule-based reasoning method to automatically generate the optimal disassembly depth. Furthermore, for the research on the disassembly depth optimization of EoL electronic products, the feasibility of model plays a significant role in determining the final research results. Therefore, it is necessary to provide a feasibility optimization model for disassembly depth optimization [17].

Currently, there are two types of optimization models within literature: one is mathematical models based on intrinsic mechanisms and the other is neural network models with multiple inputs and multiple outputs [18]. Mathematical optimization methods have been applied in manufacturing industries [19]. The mathematical models include disassembly time model [20], disassembly difficulty model [21], and disassembly profit model [22]. Xing et al. [23] established a disassembly time model considering execution time and preparation time to solve the asynchronous parallel disassembly sequence planning problem. Yang et al. [24] considered efficiency, profit, and environmental impact to establish a disassembly time, CO2 emission and recycling cost model, aimed at solving the disassembly line optimization problem of EoL products. Liu et al. [25] proposed disassembly time and profit model to improve the success rate of disassembly operation in disassembly sequence planning. Tuo et al. [26] introduced a multi-channel disassembly line balancing model considering pedestrian workers. Although the above researchers have already solved most of the problems related to disassembly optimization by establishing mathematical models, in the face of multi-objective nonlinear, or cross-domain systems, mathematical models have difficulty capturing their behaviors. Moreover, assumptions are often required to deal with complex nonlinear problems, which lead to a decrease in the accuracy and feasibility of the mathematical models [27].

Compared to mathematical models, machine learning can be effectively used to generate models to avoid the above limitations [28]. Common neural network models include an identify model based on Bayesian regularization optimization [29], non-parametric model based on improved adaptive neural network [30], and Eulerian constitutive model for rate-dependent inelasticity enhanced by neural network [31]. In addition, neural networks were used in various research areas because of their nonlinear learning, adaptive and generalization abilities [29]. The neural network model has the advantages of high identification accuracy and low cost. However, if only a single neural network model is used to solve the problem, the convergence speed is slow and the dependence on data is strong [32], which will lead to an unfeasibility model.

According to previous studies, neural networks have developed into primary optimization models for solving related optimization problems. In fact, with the rapid advancement of deep learning technology, neural networks have gradually evolved from a simple function approximation tool into a general optimization framework [33]. At present, most researchers combine optimization algorithms with neural network models to

solve the problem of model unfeasibility. Wang et al. [34] optimized the BPNN model using the Sparrow Search Algorithm, its training error and predictive error are less than 5%, and its R2 value is close to 1. Chen et al. [35] introduced the LSTM model and the BPNN model improved by SSA algorithm to predict high-complexity and low-complexity subsequences, respectively, the results show that the accuracy of the improved model can achieve to 99.17%. Through hyperparameter search, Wang et al. [36] constructed a 14-layer deep BP neural network model, SGD algorithm with Mini-batch algorithm was adopted to well balance the model performance and the training time complexity, resulting in 76.68% performance improvement and nearly 6 times training time reduction. Wu et al. [37] proposed a combined IFOA-BP neural network, the IFOA-BP model and IFOA cooperate to find the best combination of design parameters, compared with a contrastive design, the obtained optimization set of design parameters can reduce the self-weights by about 6.85%. Overall, those studies have demonstrated that optimized neural network models exhibit superior performance. However, few researchers have applied the optimized neural network model to the disassembly depth optimization research of EoL electronic products. Table 1 presents a comparison of the classical literature in the field of disassembly model establishment research in recent years.

Table 1. Comparison of classical literature in the field of disassembly model establishment.

Reference	DM		OM			Objectives					
	CD	PD	MM	NNM	INNM	DS	DE	DT	DP	DC	SI
[38]	+		+					+		+	
[39]	+		+			+		+			
[40]	+		+				+			+	
[13]		+	+			+	+	+	+		
[41]	+		+						+		+
[42]	+		+					+	+	+	
[43]	+			+		+		+			
[44]	+				+				+	+	
This study		+			+			+	+	+	

DM: disassembly model; CD: complete disassembly; PD: partial disassembly; OM: optimization model; MM: model; NNM: neural network model; INNM: improved neural network model; DS: disassembly safety; DE: disassembly energy consumption; DT: disassembly time; DP: disassembly profit; DC: disassembly carbon emissions; SI: smoothness index.

All work mentioned above has made great achievements in the field of disassembly model establishment. Most researchers choose to take the traditional mathematical model as the optimization model. However, it is difficult to fully capture their behavior in nonlinear problems for using mathematical models. In addition, the use of BPNN model lonely, due to the randomness of initial weights and biases, will cause gradient vanishing or explosion, reduce the convergence speed and predictive performance, which also affect the optimization process. To address those drawbacks, this study proposes an improved method for disassembly depth optimization of EoL electronic products based on PSO-BPNN predictive model. The PSO-BPNN predictive model is capable of rapidly fitting multiple performance metrics of disassembly depth of EoL electric products, while effectively seeking global optimized pareto solutions through intelligent optimization. This method is particularly well-suited for scenarios where multiple nonlinear objectives are mutually restrictive, making it a preferred method in current disassembly depth optimization research.

The contribution of the present work is twofold. Firstly, this study abandons the traditional mathematical modeling method and employs the PSO-BPNN model as the optimization model for disassembly depth optimization of EoL smartphones, which provides an improved method for disassembly depth optimization of EoL smartphones. Secondly, this study compared two different optimization methods and the results showed that the pareto solutions obtained by the method proposed in this study are higher quality. The proposed method provides a more reliable theoretical tool for disassembly depth optimization of EoL electronic products.

2. Disassembly depth optimization method based on PSO-BPNN model

The method proposed in this study can be divided into five main steps, as shown in Figure 1. In the first step, number the disassembly parts, construct disassembly directed graph based on actual disassembly experiment, define the disassembly constraint matrix and rules, and generate feasible disassembly depths. The second step is to optimize the initial weights and biases of the BPNN predictive model by using the PSO. In the third step, the experimental data is randomly divided into training and test sets at a rate of 7:3, the number of training iterations to 1000, the learning rate to 0.01 and the target minimum error to 1×10-5. Based on the experimental results, the PSO-BPNN model was established to predict disassembly time, profit and carbon emissions. In the fourth step, the PSO-BPNN predictive model was embedded into the Non-dominated Sorting Genetic Algorithm (NSGA-II) and used its predicted outputs as fitness values. In the fifth step, use NSGA-II for disassembly depth optimization of EoL smartphones that balance disassembly time, profit and carbon emissions.

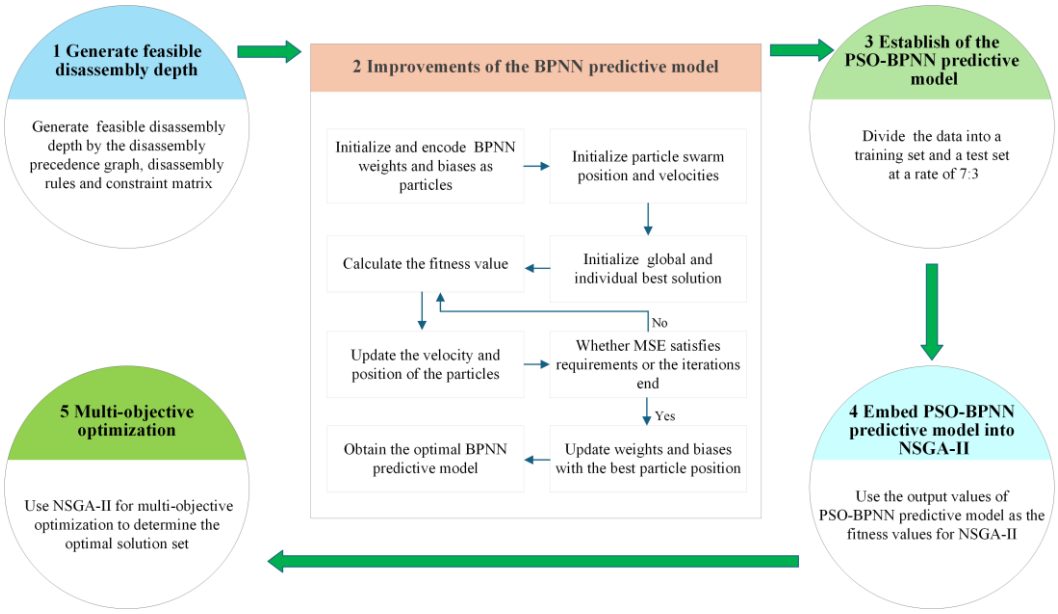

Figure 1. The flow chart of the disassembly depth optimization method.

2.1. Generate feasible disassembly depth

The disassembly precedence graph is commonly used to represent the relationships between parts of the EoL product [14], as shown in Figure 2. A single-direction arrow represents constraint relationships between parts-for example, an arrow from part 1 to part 2 means part 1 must be disassembled before part 2. A solid arc represents an 'AND' priority relationship, which means all preceding disassembly tasks to be completed before subsequent disassembly can begin. A dashed arc represents an 'OR' priority relationship, where subsequent disassembly tasks can proceed as soon as any one preceding task is

finished. The disassembly precedence graph can be represented by the constraint matrix *P*.

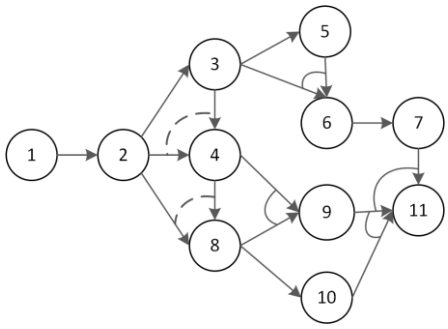

Figure 2. The disassembly precedence graph.

$$\left[P_{i,j}\right]_{11\times 11}=\begin{pmatrix} P_{1,1} & \cdots & P_{1,11} \\ \vdots & \ddots & \vdots \\ P_{11,1} & \cdots & P_{11,11} \end{pmatrix} \quad (1)$$

Use matrix *P* to describe the types of tasks, for example, $P_{1,3}$=0 indicates that part 3 cannot be disassembled after removing part 1; $P_{1,2}$=1 means part 2 can be disassembled once part 1 is removed; $P_{2,4}$=2 shows that part 4 can be selectively disassembled after removing part 2.

The disassembly rules of EoL smartphones were established as follows [13]: (1) disassembly parts with high recycling value; (2) disassembly parts with high environmental pollution impact; (3) disassembly parts that require the same disassembly tool; (4) disassembly parts with the same attributes.

2.2. *Improvements of the BPNN predictive model*

The BPNN model mainly consists of input layer, hidden layers, and output layer [27]. Random initial weights and biases in BPNN predictive model often results in slow convergence speed, high MSE, and prediction inaccuracies. Therefore, this study uses PSO to optimize the weights and biases of the BPNN predictive model. Figure 3 illustrates the topological structure graph of the PSO-BPNN model.

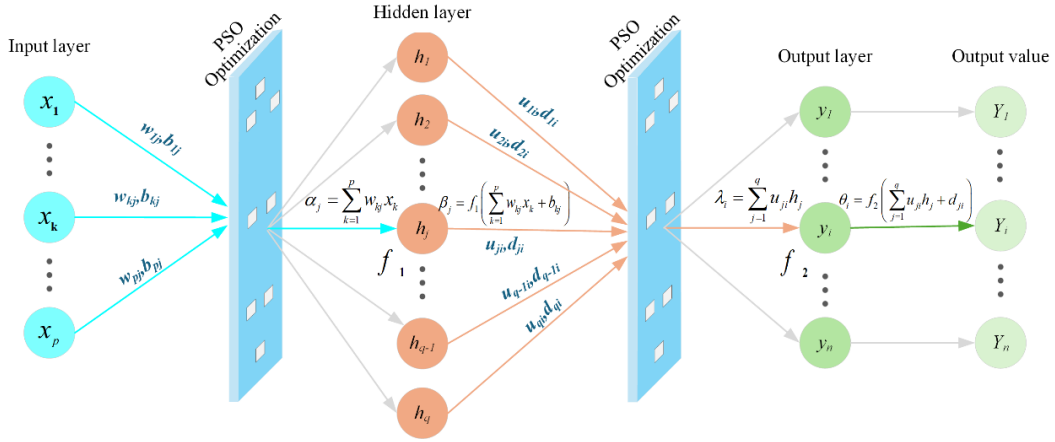

Figure 3. PSO-BPNN predictive model topological structure graph.

From Figure 3, the computational principle of BPNN can be observed [30]. The network processes *P* independent input variables through an initial weighting operation using weight matrix *W*= [w_{11}, w_{12}, …, w_{jk}, …, w_{pq}] and biases vector *B*= [b_{11}, b_{12}, …, b_{kj}, …, b_{pq}]. These

weighted inputs then pass through hidden layer neurons, where activation function f_1 transforms the signals. Similarly, the output layer subsequently performs another weighted summation using weight matrix U= [u_{11}, u_{12}, …, u_{ji}, …, u_{qs}], biases vector D= [d_{11}, d_{12}, …, d_{ji}, …, d_{qs}], followed by transformation through activation function f_2. For both layers, the Sigmoid function is employed as the nonlinear activation operator.

$$f_{1,2}(x) = Sigmoid(x) = \frac{1}{1+e^{-x}} \quad (2)$$

The input and output of the *j-th* hidden layer neuron and the *i-th* output layer neuron can be calculated using equations (3)-(6).

$$\alpha_j = \sum_{k=1}^{p} w_{kj} x_k \quad (3)$$

$$\beta_j = f_1\left(\sum_{k=1}^{p} w_{kj} x_k + b_{kj}\right) \quad (4)$$

$$\beta_j = f_1\left(\sum_{k=1}^{p} w_{kj} x_k + b_{kj}\right) \quad (5)$$

$$\theta_i = f_2\left(\sum_{j=1}^{q} u_{ji} h_j + d_{ji}\right) \quad (6)$$

where p represents the number of input layer neurons, q represents the number of hidden layer neurons, and x_k is the value of *k-th* input layer neuron (k = *1*, …, p). The connection between input and hidden layers is characterized by weights w_{jk} and biases b_{jk}, which links the *k-th* input layer neuron to the *j-th* hidden layer neuron. Similarly, h_j is the value of *j-th* input hidden layer neuron (j=*1*, …, q), u_{ij} and d_{ji} are the weights and biases from the *j-th* hidden layer neuron to the *i-th* output layer neuron, respectively. The weight matrices can be represented by equations (7), (8).

$$q_1 = \begin{pmatrix} w_{11} & \cdots & w_{1q} \\ \vdots & \ddots & \vdots \\ w_{p1} & \cdots & w_{pq} \end{pmatrix} \quad (7)$$

$$q_2 = \begin{pmatrix} u_{11} & \cdots & u_{1n} \\ \vdots & \ddots & \vdots \\ u_{q1} & \cdots & u_{qn} \end{pmatrix} \quad (8)$$

where q_1 is the weights matrix from the input layer to the hidden layer, and q_2 is the weights matrix from the hidden layer to the output layer. In addition, the number of neurons in the input and output layers of BPNN is determined by variable dimensions, and the number of hidden layer neuron is usually determined based on empirical formulas (9).

$$s = \sqrt{n+l} + a \quad (9)$$

where a is a constant ranging from [1, 10], l is the number of neurons in the output layer and n is the number of neurons in the input layer.

After model training, the predictive performance of the PSO-BPNN model is typically evaluated using MSE [45]. MSE quantifies the average squared difference between the predicted values and the actual values of model, which serve as a key indicator for assessing prediction accuracy. Lower MSE indicates better model performance and higher prediction accuracy.

$$MSE = \frac{1}{n}\sum_{i=1}^{n}\left(Y_i - y_i\right)^2 \quad (10)$$

where Y_i is the actual value, y_i is the predicted value from the model, and n is the number of samples.

The MSE is used as the objective function for PSO, which iteratively optimizes the weights and biases of BPNN. The optimization procedure consists of the following steps.

Step 1: The weights and biases of the BPNN are encoded as particles. The positions xi and velocities vi of the particle swarm are initialized, with each particle representing a BPNN predictive model. The position represents a combination of weight and biases.

Step 2: Initialize the global best solution (p_g) and the individual best solution (p_i), which represents the optimal solution of the particle swarm and each individual particle, respectively.

Step 3: Use the MSE of the BPNN as the fitness function to calculate the fitness value of each particle.

Step 4: Based on the individual best solution and the global best solution of particles, combined with the inertia weights (w), learning factors (c_1, c_2), and random numbers (r_1, r_2). The new velocity and position are calculated by equation [46].

$$\begin{cases} v_i^{k+1} = \omega v_i^k + c_1 r_1 (p_i - x_i^k) + c_2 r_2 (p_g - x_i^k) \\ x_i^{k+1} = x_i^k + v_i^{k+1} \end{cases} \quad (11)$$

where v_i^k and x_i^k represents the velocity and position (combination of weights and biases) of particle i in the k-th generation, respectively.

Step 5: Update the global best solution and individual best solution based on the fitness values. If the fitness value of a particle is better than the global best solution, update the global best solution; otherwise, update the individual best solution.

Step 6: If the MSE satisfies the defined requirements or the iterations end, output the current best position as the optimal weights and biases of the BPNN predictive model; otherwise, return to step 4 and continue the iteration.

Step 7: The optimal weights and biases are assigned to the BPNN predictive model, if the MSE satisfies the defined requirements, output the predictive value; otherwise, return to step 1.

2.3. Establishment of the PSO-BPNN predictive model

The PSO is used in the traditional BPNN predictive model to optimize the weights and biases of the model. Firstly, the network structure needs to be determined, which includes the number of neurons in the input layer, hidden layer, and output layer. Secondly, initialize the particle swarm, where each particle represents the weights and biases of the BPNN predictive model, randomly generated the initial values to ensure diversity. During training, MSE is used as an evaluation index to measure the performance of the network on the training data, which served as the objective function of PSO. Finally, through iterative optimization, the network tended to the optimal weights and biases, and the optimal weights and biases were assigned to BPNN predictive model.

The number of input layer neurons correspond to the relevant features variables in the problem domain. For disassembly depth optimization of EoL smartphones, the input layer features include basic disassembly time, disassembly cost, part recovery price, part recovery rate, indirect carbon emissions, and sorting time. Therefore, the number of input layer neuron x_p is set to 6. The number of output layer neurons depends on the predictive targets. In this study, the output layer is defined to include disassembly time, profit, and carbon emissions. Therefore, the number of output layer neuron y_n is set to 3. The number of hidden layer neuron h_q is determined to be 6 based on equation (9). The 150 experimental data samples are randomly divided into training and testing set at a ratio of 7:3, which aim to better train the model. The neural network employs Sigmoid activation function across all layers, with hidden layer training performed through the Levenberg-Marquardt algorithm. The training process is configured with a maximum of 1000 iterations

with a learning rate of 0.01, and the target minimum error is 1×10-5 to ensure optimal model performance while preventing overfitting.

Accordingly, a 6-6-3 BPNN predictive model is established. The established BPNN predictive model adjusts the weights and biases of each neuron through feedback from the error function, which enables it to produce outputs similar to the expected target distribution.

2.4. Embed the PSO-BPNNpredictive model into NSGA-II

The PSO-BPNN predictive model demonstrates strong learning and generalization ability, and the accuracy of the prediction of disassembly time, profit and carbon emissions has also been improved. As shown in Figure 4, the trained PSO-BPNN predictive model generated predictive outputs (disassembly time, profit, and carbon emissions) for each disassembly depth, which serve as the objective functions for the subsequent NSGA-II optimization process.

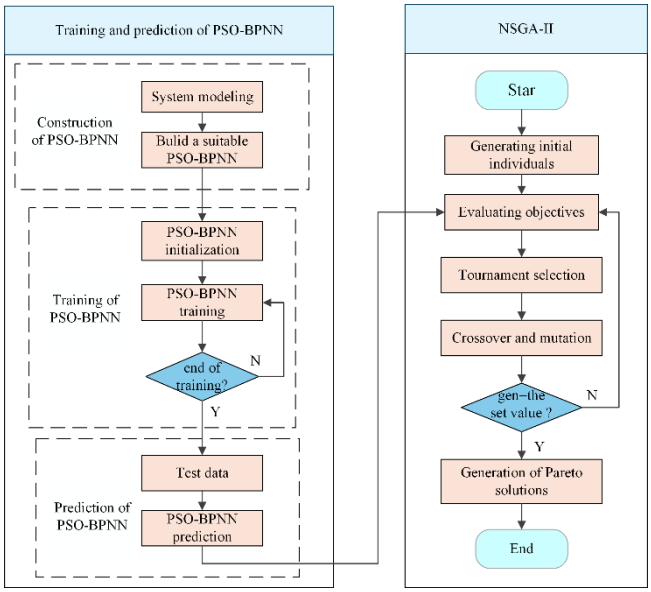

Figure 4. The algorithm flow chart of embedding PSO-BPNN into NSGA-II.

NSGA-II introduces the elite retention strategy based on the original NSGA to prevent the loss of excellent individuals during the evolution process and improve the convergence of the algorithm [47]. In addition, NSGA-II does not require the pre-allocation of weights for each objective function, which avoids the subjectivity of weight selection and makes it applicable to a wider range of problems. The main steps for the PSO-BPNN predictive model to be embedded into NAGA-II are as follows.

Step 1: Establish the predictive model for disassembly time, profit, and carbon emissions, respectively.

Step 2: Train the PSO-BPNN predictive model until iteration ends or MSE satisfies the defined requirements.

Step 3: The trained PSO-BPNN predictive model generates output predicted results: disassembly time, profit, and carbon emissions.

Step 4: NSGA-II randomly generates the initial population, with the first generation selected randomly within the variable range.

Step 5: The PSO-BPNN prediction results serve as the fitness values of individuals in the optimization process.

Step 6: Calculate the crowding distance of each individual to preserve solution diversity along the pareto front. Individuals with larger crowding distances are given higher

selection priority, as they represent less densely populated regions of the objective space. The calculation formula is as follows.

$$d_i = \sum_{m-1}^{M} \left(\frac{f_m(i+1) - f_m(i-1)}{f_m^{\max} - f_m^{\min}} \right) \quad (12)$$

where d_i is the crowding distances of individual i, $f_m(i\text{-}1)$ and f_m $(i\text{+}1)$ are the objective values of the neighboring individuals; where $f_m^{\max}$ and $f_m^{\min}$ are the maximum and minimum values of the objective, respectively.

Step 7: Select individuals based on fitness values and crowding distance, with priority given to those with higher fitness and smaller crowding distances for the next generation.

Step 8: Perform crossover and mutation to generate better solutions. If the crossover occurs at positions k1 and k2, the formula is as follows.

$$\begin{cases} O_1 = \left[x_1^1, \ldots, x_{k_1}^1, x_{k_1+1}^2, \ldots, x_{k_2}^2, x_{k_2+1}^1, \ldots, x_n^1 \right] \\ O_2 = \left[x_1^2, \ldots, x_{k_1}^2, x_{k_1+1}^1, \ldots, x_{k_2}^1, x_{k_2+1}^2, \ldots, x_n^2 \right] \end{cases} \quad (13)$$

where O1 and O2 represent the parent individuals.

Step 9: To obtain the pareto solutions, repeat steps 6 to 8 until the iteration ends.

2.5. Multi-objective optimization

In consideration of the practical circumstances of relevant disassembly companies, the disassembly time, profit, and carbon emissions were used as optimization objectives in this study. There are conflicts between optimization objectives. To present the optimal solutions obtained more clearly, the NSGA-II is used to seek the pareto front. Disassembly time is calculated by the weighted sum of the times for each stage, disassembly profit is based on the value of recovered parts, recovery rates, and costs, and disassembly carbon emissions is estimated based on energy consumption. To achieve better convergence on the pareto front, an appropriate number of iterations and population size are necessary [48]. The initial population size is set to 20 to ensure sufficient diversity. The iterations of NSGA-II are set to 100 to enable the algorithm to search effectively and converge on suitable solutions. The crossover and mutation probabilities are set to 0.9 and 0.1, respectively.

Commonly, the maximum disassembly profit is the desired outcome. However, in multi-objective optimization problems, objectives are typically minimized, therefore, the reciprocal is used as the optimization objective. The pareto optimization problem is formulated as follows.

$$\min f(x) = \min \left[T, \frac{1}{P}, E \right] \quad (14)$$

where T, P, and E represent disassembly time, disassembly profit, and disassembly carbon emissions, respectively.

3. Case study

The EoL smartphone, namely 'Huawei P7', is used as an example to verify the feasibility of the proposed method. The PSO-BPNN and BPNN predictive model are used to predict disassembly time, profit, and carbon emissions respectively. Combined with NSGA-II, the predictive output of the model is optimized, and the feasibility of the proposed method is verified.

3.1. Fundamental data

The disassembly parts graph for 'Huawei P7' is shown in Figure 5, which contains 12main parts of 'Huawei P7' and their numbers. The precedence graph of 'Huawei P7' shows the precedence constraint relationship between the 12 main parts, as shown in Figure 6. In addition, the data in this study are derived from actual disassembly experiments

and market research. Due to the relative comparison being used, the research results are not affected by part recovery prices. The disassembly tool information is shown in Table 2, and the tool damage cost is estimated using the wholesale purchase prices and service life statistics [13]. The basic disassembly information of 'Huawei P7' is shown in Table 3, which includes part market recovery rates, recovery prices, and other relevant parameters. Table 4 lists the relevant carbon emission factors [49], which mainly consider the fuel consumption of material transportation and electricity consumption for equipment operation.

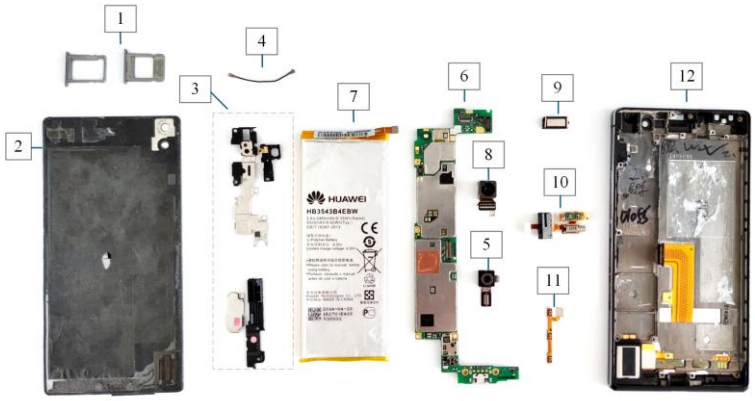

Figure 5. Disassembly parts graph of 'Huawei P7'.

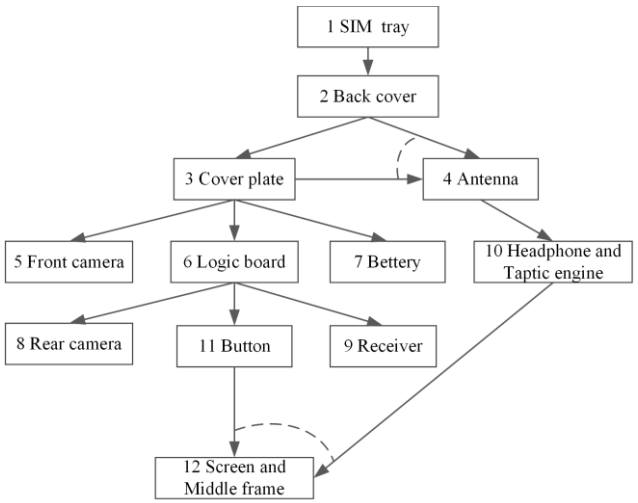

Figure 6. The Disassembly precedence graph of 'Huawei P7'.

Table 2. Disassembly tool information.

Tool Name	Tool operational parameters	The tool damage cost for each use
Electric screw bit	Power: 50 w; Rotational speed: 500r/min	0.01
Hot air gun	Power: 600 w; Heating temperature: 100℃	0.01
SIM-ejector tool	Moving speed: 0.5m/s	0.005
ESD-safe tweezer	Moving speed: 0.5m/s	0.005
Black stick	Moving speed: 0.5m/s	0.005

Table 3. The basic disassembly information of 'Huawei P7'.

Part NO.	Part Name	Connection method of parts	Disassembly tools and usage sequence	disassembly direction	Market recovery rate	Market recovery price (¥)
1	SIM tray	Insert	SIM-ejector tool	-Y	95%	0.5
2	Back cover	Adhesive	Hot air gun → Black stick	+Z	95%	0.5
3	Cover plate	Screws + Buckle	Electric screw bit	+Z	95%	5
4	Antenna	Snap-fit	Black stick	+Z	95%	1
5	Front camera	Clip-on Connector	Black stick	+Z	98%	15
6	Logic board	Screws + Snap-fit	Electric screw bit → Black stick	+Z	99%	45
7	Battery	Adhesive	Hot air gun → Black stick	+Z	99%	20
8	Rear camera	Clip-on Connector	Black stick	+Z	98%	20
9	Receiver	Adhesive	ESD-safe tweezer	+Z	95%	0.5
10	Headphone and Taptic engine	Adhesive + Snap-fit	Black stick	+Z	95%	0.5
11	Button	Adhesive + Snap-fit	ESD-safe tweezer	+Z	95%	0.5
12	Screen and Middle frame	Adhesive	Hot air gun → Black stick → ESD-safe tweezer	-Z	98%	1.5

Table 4. Carbon emissions factor of different sources.

Energy type	Utilization	Carbon emission factors
Electrical energy	Power consumption of equipment	0.5kg/kw h
Diesel fuel	Power consumption of material transportation	2.31kg/L
Gasoline	Power consumption of material transportation	3.68kg/L

The disassembly time is measured using a stopwatch, and the disassembly carbon emissions and disassembly cost are calculated by equations (15) and (16).

$$E_{co_2} = M \times C \quad (15)$$

$$N = \sum_{l=1}^{q} (u_l \times g_l) + N_2 + N_3 + N_4 \quad (16)$$

where M represents energy consumption, C is the carbon emission factor, and q is the number of disassembly tools used, u_l is the number of times each smartphone uses tool l, and g_l is the tool damage cost of using tool l once.

3.2. Figures, Tables and Schemes

Based on the basic disassembly information of 'Huawei P7', the disassembly precedence graph, and the disassembly rules, the feasible disassembly depth be generated. As shown in Figure. 7, to avoid experimental randomness, three personnel with experience in EoL smartphones disassembly were selected to conduct the experiment simultaneously, and the disassembly data were recorded respectively. In the data processing procedure, to reduce experimental costs and generate irregular samples, Latin Hypercube Sampling (LHS) was used to randomly select 50 sets of disassembly depths [50]. The LHS design is formulated as shown in equation (17).

$$x_j^{(i)} = \frac{\pi_j^{(i)} + U_j^{(i)}}{n_s} \quad ,1 \le j \le n_s, \quad 1 \le i \le n_s \tag{17}$$

where i is the *i-th* sample, j is the *j-th* component of *j-th* sample, U_j is taken from the range [0,1], n_s is the number of sample points, and its value is a random number from [0, n-1].

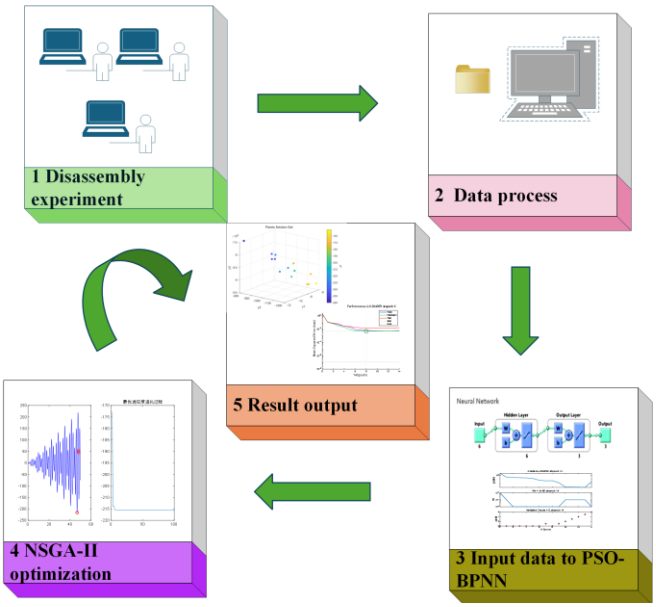

Figure 7. The application flow chart of proposed method in the case study'.

The basic disassembly time, disassembly cost, part recovery price, part recovery rate, indirect carbon emissions, and sorting time are all important factors, therefore, they are taken as the input of the neural network. Then, the processed data is input into the PSO-BPNN predictive model, and the predicted results are used as the individual fitness value for NSGA-II optimization. Finally, the pareto solutions were obtained.

4. Results and discussion

Firstly, this section discusses the predictive performance of the PSO-BPNN predictive model for the disassembly time, profit, and carbon emissions of EoL smartphones. Comparative analysis demonstrates that the superior performance of PSO-BPNN predictive model is better than BPNN predictive model. Secondly, for the disassembly depth optimization of EoL smartphones, the superior pareto solutions are obtained by the proposed method.

4.1. Discussion for prediction results of the PSO-BPNN predictive model

Three groups of experiments were conducted to verify the predictive performance of PSO-BPNN predictive model.

In the first experimental group, 150 sets of data were selected, and the training set and the test set were divided into a ratio of 7:3 for verification. The input and output samples were trained by the PSO-BPNN and BPNN predictive model to establish the network relationships between inputs and corresponding outputs. Figure. 8 shows the disassembly time prediction results for both models on the test set. As shown in Figure. 8a, the BPNN predictive model exhibits significant prediction bias for samples 43 to 45. In contrast, Figure. 8b shows that the PSO-BPNN predictive model maintains strong agreement between the predictive values and actual values across all samples. According to equation (10), the MSE values for BPNN and PSO-BPNN predictive model are calculated as 58.022 and 4.083, respectively. Compared to the BPNN predictive model, the PSO-BPNN predictive model

achieves an approximately 92.95% reduction in MSE. Therefore, the predictive model established based on PSO-BPNN was effective in the first group experiment.

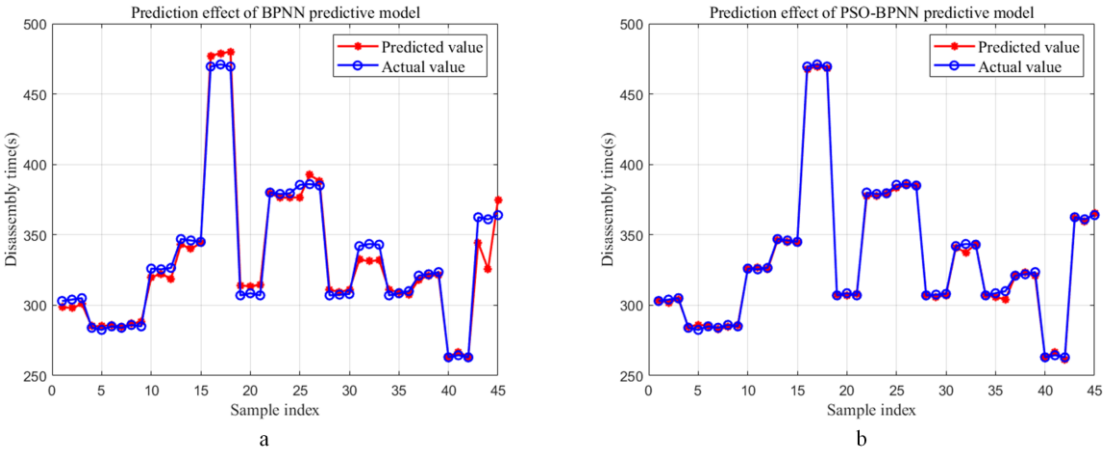

Figure 8. Disassembly time prediction results (a BPNN; b PSO-BPNN).

The same procedure was applied to the second and third sample groups, and similar results were obtained, Compared with BPNN predictive model, the PSO-BPNN predictive model still maintains relatively high accuracy, which further verified the predictive performance of PSO-BPNN predictive model for both disassembly profit and carbon emissions. Figure. 9 and Figure. 10 show the results of the second and third experiments, respectively. The quantitative analysis shows that for disassembly profit prediction, the MSE values are 12.422 (BPNN) and 0.433 (PSO-BPNN), which represents an approximately 96.51% reduction. Similarly, for carbon emission prediction, the corresponding MSE values are 13.178 (BPNN) and 0.956 (PSO-BPNN), which demonstrates an approximately 92.74% reduction. From Figure. 11, R^2 of PSO-BPNN predictive model reaches 0.9964, 0.9946, 0.9936 for disassembly time, disassembly profit and disassembly carbon emissions, respectively, higher than that of BPNN predictive model (0.9779, 0.9713, 0.9785). Although both models have been fully trained, the PSO-BPNN predictive model has an excellent predictive ability for this study case. Besides, all prediction accuracy is also higher than trusted value (R^2=0.9092) in the literature [46]. Therefore, the PSO-BPNN predictive model could be accepted as the optimization model for subsequent disassembly depth optimization.

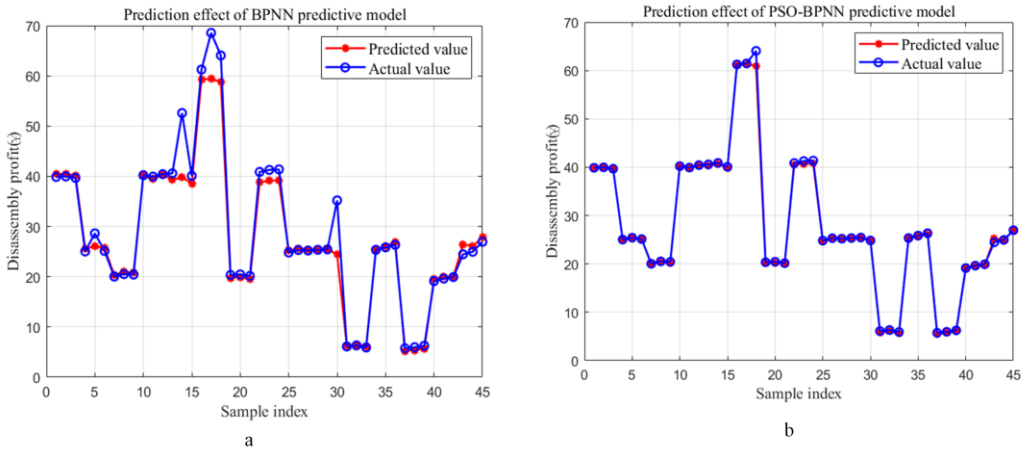

Figure 9. Disassembly profit prediction results (a BPNN; b PSO-BPNN).

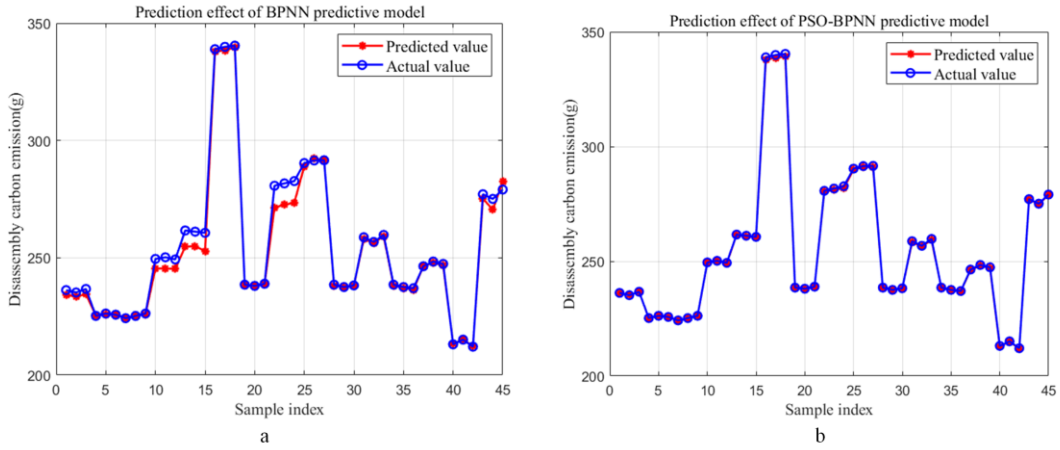

Figure 10. Disassembly carbon emissions prediction results (a BPNN; b PSO-BPNN).

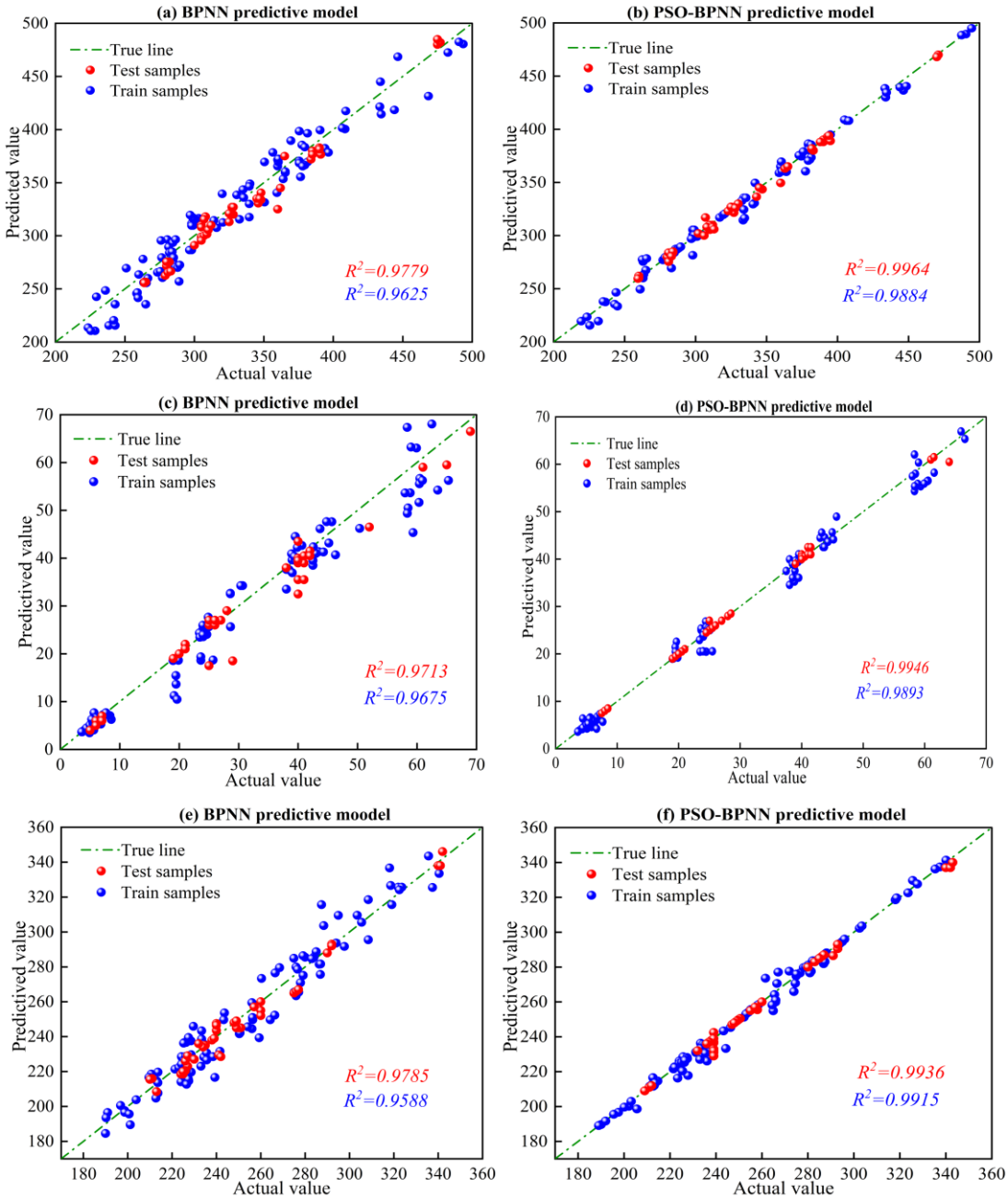

Figure 11. Comparison in regression between BPNN and PSO-BPNN.

(a) Regression of BPNN for disassembly time; (b) Regression of PSO-BPNN for disassembly time

(c) Regression of BPNN for disassembly profit; (d) Regression of PSO-BPNN for disassembly profit

(e) Regression of BPNN for disassembly carbon emissions; (f) Regression of PSO-BPNN for disassembly carbon emissions

The accuracy of PSO-BPNN predictive model for disassembly time, disassembly profit and disassembly carbon emissions does not reach 100% for some reasons. Firstly, as a data -driven approximate model, the predictive ability of PSO-BPNN is limited by the network structure and optimization algorithms. If the number of network layers is too small or the number of neurons is insufficient, the model may not be able to fully learn complex data patterns, and the network may not converge. Secondly, the small number of samples may result in poor model training with regard to predictive ability.

4.2. Discussion for the pareto optimal solutions

This section presents and compares the disassembly depth optimization results obtained from both BPNN optimization method and the proposed method in this study. Figure 12 presents the pareto solutions obtained by both methods. Specifically, Figure 12a shows those obtained by traditional BPNN optimization method, while Figure 12b shows the pareto solution obtained by proposed method in this study. The circular markers in the figure represent different disassembly depths. For easy analysis, the pareto solutions were divided into two groups: group A (traditional BPNN optimization method) and group B (proposed method in this study). Table 5 shows the results of disassembly depth optimization for the EoL smartphone 'Huawei P7'.

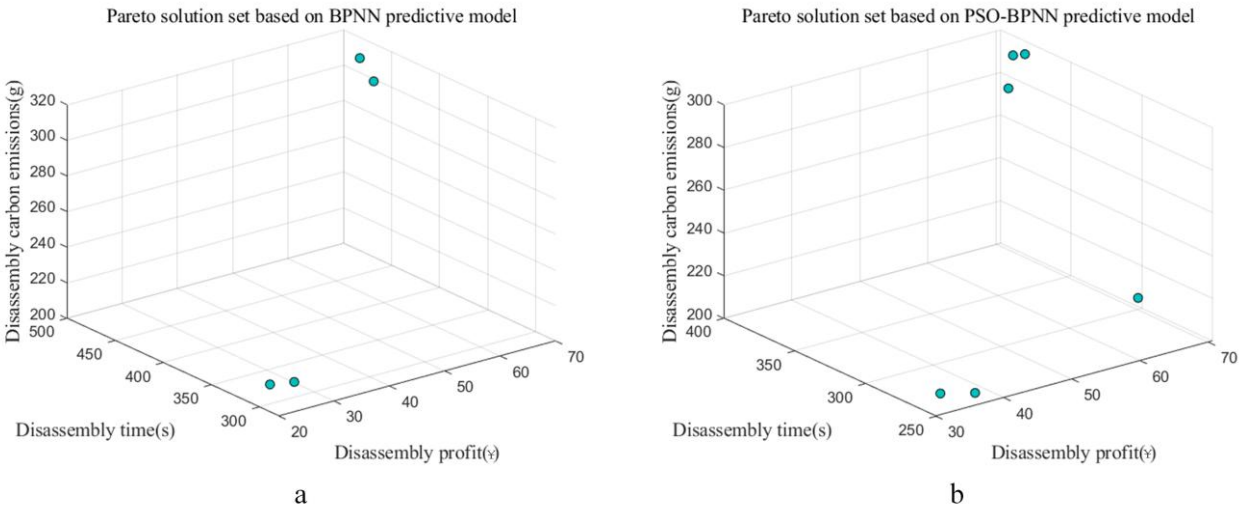

Figure 12. The spatial distribution of pareto solution (a BPNN; b PSO-BPNN).

The two pareto solution sets show that the overall quality of the solution and various optimization indictors are all different. Particularly, in terms of the disassembly time and disassembly carbon emission, the method proposed in this study has shown significant improvements. As the optimization results shown in Table 5, compared to group A, the number of non-inferior solutions in group B increased by 5, while the number of optimized solutions increased by 3, and shows superior overall solution quality. Although the top three disassembly depths in group A and group B are the same, the overall performance indicators in group B are significantly better than those in group A: a 16.8% reduction in disassembly time, 6.45% lower carbon emissions, and a 53.54% increase in disassembly profit compared to group A. Another interesting result is observed from analyzing the third disassembly depth of the two groups, which get the same disassembly profit in both groups, group B demonstrates 17.1% shorter disassembly time, and 7.8% lower

carbon emissions compared to group A. The reason for the above results can be attributed to the unfeasibility of the optimization model, which failed to fully capture the target information, resulting in inaccurate predictions and causing errors in the subsequent disassembly depth optimization process.

Table 5. Comparison of disassembly depth optimization results.

Group number	NO.	The Disassembly depth	Disassembly time(s)	Disassembly profit(￥)	Disassembly carbon emissions(g)	The non-inferior solution	The optimized solution
A	1	1-2-3-5-6-7-8	279.5	22.72	218.6	×	×
	2	1-2-3-6-8-5	290.5	20.39	217.7	×	×
	3	1-2-3-6-10-5-8-7-11-12	471.5	70.58	315.6	×	×
	4	1-2-3-5-6-8-11-12	416.5	60.98	319.4	√	×
B	1	1-2-3-5-6-7-8	221.5	63.19	207.8	√	√
	2	1-2-3-6-8-5	254.5	36.94	204.9	√	×
	3	1-2-3-6-10-5-8-7-11-12	390.5	70.58	290.7	√	√
	4	1-2-3-6-7-5-8-9-11-12	382.5	70.31	293.8	√	√
	5	1-2-3-6-5-7-8-11-9-12	368.5	64.90	287.3	√	×
	6	1-2-3-6-7-8	264.3	33.62	203.1	√	×

To further verify the feasibility of the proposed method in this study, the disassembly time, disassembly profit and disassembly carbon emissions were selected as optimization objectives and iterated 100 times. The results shown as in Figure 13, Figure 14 and Figure 15, respectively.

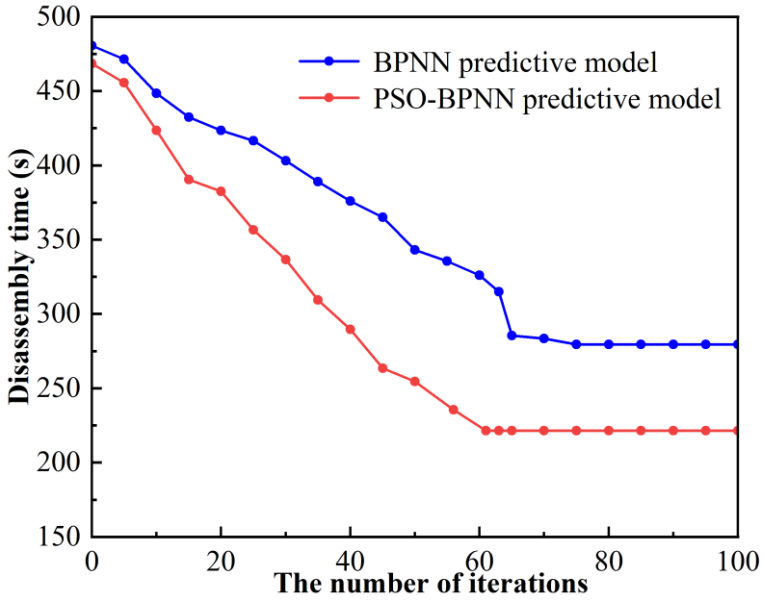

Figure 13. The iteration graph of disassembly time.

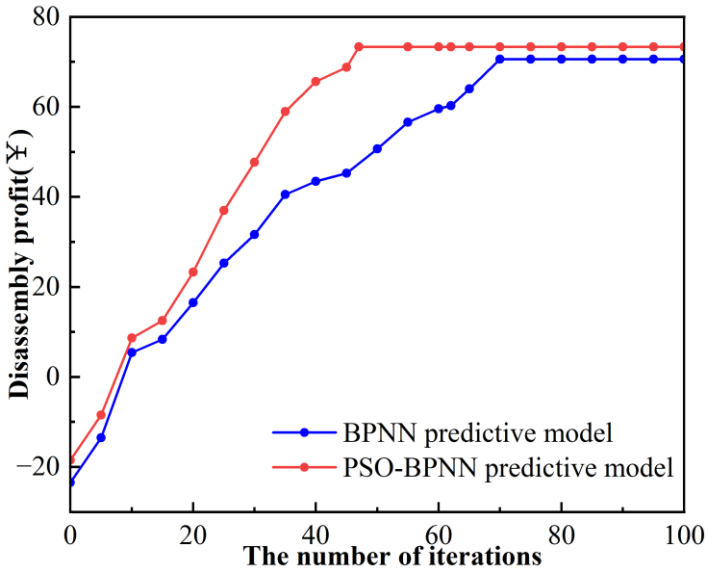

Figure 14. The iteration graph of disassembly profit.

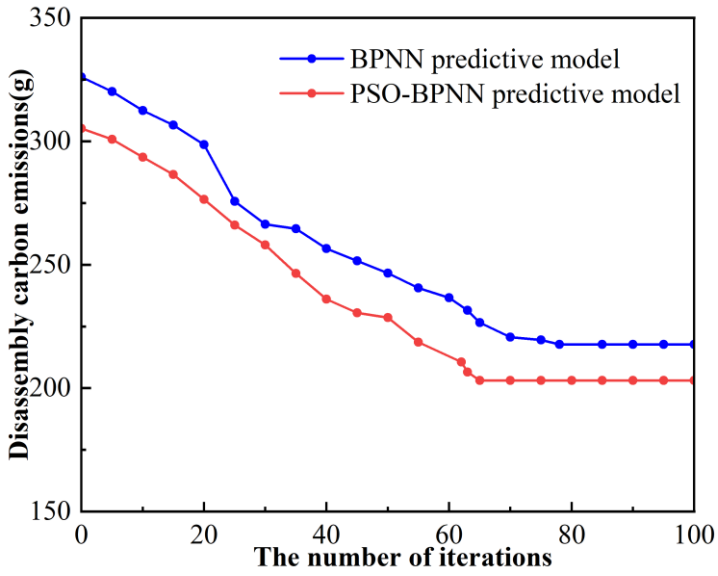

Figure 15. The iteration graph of disassembly carbon emissions.

During the process of searching for the optimized solutions of disassembly time, as shown in Figure 13, the PSO-BPNN predictive model tends to converge at *61-th* generation, compared to *75-th* generation for the BPNN predictive model, which represents an 18.6% improvement in convergence speed. Figure 14 shows that in the process of searching for optimized disassembly profit, the PSO-BPNN predictive model converges at *47-th* generation, compared to *70-th* generation for the BPNN predictive model, which represents a 32.8% improvement in convergence speed. Figure 15 shows that in the process of searching for optimized disassembly carbon emissions, the PSO-BPNN predictive model converges at *65-th* generation, compared to *78-th* generation for the BPNN predictive model, which represents a 16.6% improvement in convergence speed.

4.3. The limitations

The proposed method in this study provides a reference direction for the disassembly of EoL electronic products, combined with multi-objective optimization algorithm and deep learning model. However, there are also some limitations. Firstly, the definition of

the disassembly rules is based on the needs of most disassembly companies, which potentially limit their generalizability. Secondly, although the combination of BPNN and NSGA-II shows effective optimization ability during the optimization process, there is still room for improvement in terms of fitness function design, data quality, and algorithm efficiency. Finally, the dataset adequately represents the diversity of the disassembly process, the dataset size can be further expanded to enhance the generalization capability of model.

5. Conclusions

In this study, an improved method based on PSO-BPNN predictive model is proposed, which aims to shorten disassembly time, reduce disassembly carbon emissions, and increase disassembly profit. The PSO-BPNN model directly responds to the traditional neural network and mathematical model lacks accuracy in face of multi-objective nonlinear problems. Then, the feasibility of the proposed method is verified by 'Huawei P7' disassembly case. Compared to BPNN predictive model, the PSO-BPNN predictive model significantly reduced MSE approximately 92.95% for disassembly time, 96.51% for disassembly profit, and 92.74% for disassembly carbon emissions, which demonstrate superior performance and provides feasible optimization model for disassembly depth optimization. Based on the PSO-BPNN predictive model, the proposed method maintains disassembly profit while reducing disassembly time and disassembly carbon emissions by 17.1% and 7.8%, respectively. Additionally, the convergence speed of PSO-BPNN predictive model search for optimal solution in disassembly time, disassembly profit, and disassembly carbon emissions increased by 18.6%, 32.8% and 16.6%, respectively. In summary, the proposed method provides high-quality pareto solutions and offers a reference for the research on the disassembly of EoL electronic products.

In future research, additional optimization objectives such as disassembly complexity and remanufacturing potential can be considered. In addition, other more superior network models can also be considered for optimization.

Author Contributions: conceptualization, S.J., L.L. and Y.Y.; methodology, S.J. and L.L.; software, S.J.; validation, S.J.; formal analysis, L.L., F.Y. and Y.Y.; investigation, L.L., Y.Y., F.Y.; resources, Y.Y. and F.Y.; data curation, L.L., Y.Y., F.Y. Y.; writing—original draft preparation, S.J.; writing—review and editing, L.L. and F.Y.; supervision, L.L. and F.Y.; project administration, L.L. and F.Y.; funding acquisition, L.L. All authors have read and agreed to the published version of the manuscript.

Funding: This work was supported by the National Key Research and Development Program of China (grant number 2020YFB1713001).

Institutional Review Board Statement: Not applicable

Informed Consent Statement: Not applicable

Data Availability Statement: Data will be made available on request.

Acknowledgments: The authors wish to thank Huaqing Li for his guidance with the BPNN model and Xiaojing Chu for her help in collecting the disassembly experiment data.

Conflicts of Interest: The authors declare no conflict of interest. The funders had no role in the design of the study; in the collection, analyses, or interpretation of data; in the writing of the manuscript; or in the decision to publish the results.

References

1. Zeng, Y.; Zhang, Z.; Yin, T.; Zheng, H. Robotic disassembly line balancing and sequencing problem considering energy-saving and high-profit for waste household appliances. *J Clean Prod*. 2022, 381, 135209. https://doi.org/10.1016/j.jclepro.2022.135209.

2. Sun, B.; Li, B.; Ma, S.; Zhu, M.; Dong, C.; Xiang, M.; Cheng, H.; Yu, Y. The recycling potential of unregulated waste electrical and electronic equipment in China: Generation, economic value, and cost-benefit analysis. *J Clean Prod*. 2023, 402, 136702. https://doi.org/10.1016/j.jclepro.2023.136702.
3. Wu, C.; Shi, Y.; Arthanari, T.; Gao, Y.; Li, X. Examining the Chinese mobile phone industry in the reverse supply chains. *Comput Ind Eng*. 2022, 82, 109407. https://doi.org/10.1016/j.cie.2023.109407.
4. Gulivindala, AK.; Bahubalendruni, MVAR.; P, MB.; Eswaran, M. Mechanical disassembly sequence planning for end-of-life products to maximize recyclability. *Sādhanā*. 2023, 48, 109. https://doi.org/10.1007/s12046-023-02160-w.
5. Wang, N.; Wu, Q.; Wang, M.; He, D.; Fang, H. A novel recycling method using machine vision to assist in the processing of stacked waste fans. *J Mater Cycles Waste Manage*. 2024, 26, 1649-1666. https://doi.org/10.1007/s10163-023-01718-4.
6. Clegg, AJ.; Williams, DJ. The strategic and competitive implications of recycling and design for disassembly in the electronics industry. *IEEE*. 1994, 33, 6-12. https://doi.org/10.1109/isee.1994.337272.
7. Dillon, PS. Salvageability by design. *IEEE Spectrum* 1994, 31, 18-21. https://doi.org/10.1109/6.299530.
8. Paterson, DAP.; Ijomah, WL.; Windmill, JFC. End-of-life decision tool with emphasis on remanufacturing. *J Clean Prod*. 2017, 148, 653-664. http://dx.doi.org/10.1016/j.jclepro.2017.02.011.
9. Wang, K.; Li, X.; Gao, L. Modeling and optimization of multi-objective partial disassembly line balancing problem considering hazard and profit. *J Clean Prod*. 2019, 211, 115-133. https://doi.org/10.1016/j.jclepro.2018.11.114.
10. Bentaha, ML.; Dolgui, A.; Battaïa, O.; Hu, J. Profit-oriented partial disassembly line design: dealing with hazardous parts and task processing times uncertainty. *Int J Prod Res*. 2018, 56, 7220-7242. https://doi.org/10.1080/00207543.2017.1418987.
11. Yin, T.; Zhang, Z.; Jiang, J. A Pareto-discrete hummingbird algorithm for partial sequence-dependent disassembly line balancing problem considering tool requirements. *J Manuf Syst*. 2021, 60, 406-428. https://doi.org/10.1016/j.jmsy.2021.07.005.
12. Yin, T.; Zhang, Z.; Wu, T.; Zeng, Y.; Zhang, Y.; Liu, J. Multimanned partial disassembly line balancing optimization considering end-of-life states of products and skill differences of workers. *J Manuf Syst*. 2023, 66, 107-126. https://doi.org/10.1016/j.jmsy.2022.12.002.
13. Chen, Z.; Li, L.; Chu, X.; Yin, F.; Li, H. Multi-Objective Disassembly Depth Optimization for End-of-Life Smartphones Considering the Overall Safety of the Disassembly Process. *Sustainability* 2024, 16, 1114. https://doi.org/10.3390/su16031114.
14. Wu, S.; Noronha, FP.; Kwade, A.; Droder, K. Advancing Material Separation Efficiency Through Extended Disassembly Depth in Pretreatment Processes for Lithium-ion Batteries Recycling. *Procedia CIRP*. 2024, 127, 255-260. https://doi.org/10.1016/j.procir.2024.07.044.
15. Gao, J.; Wang, G.; Xiao, J.; Zheng, P.; Pei, E. Partially observable deep reinforcement learning for multi-agent strategy optimization of human-robot collaborative disassembly: A case of retired electric vehicle battery. Robot *Comput-Integr Manuf*. 2024, 89, 102775. https://doi.org/10.1016/j.rcim.2024.102775.
16. Hu, Y.; Liu, C.; Zhang, M.; Lu, Y.; Jia, Y.; Xu, Y. An ontology and rule-based method for human–robot collaborative disassembly planning in smart remanufacturing. *Robot Comput-Integr Manuf*. 2024, 89, 102766. https://doi.org/10.1016/j.rcim.2024.102766.
17. Li; L.; Yan, J.; Xing, Z. Energy requirements evaluation of milling machines based on thermal equilibrium and empirical modelling. *J Clean Prod*. 2013, 52, 113-121. http://dx.doi.org/10.1016/j.jclepro.2013.02.039.
18. Chai, K.; Xia, W.; Shen, R.; Luo, G.; Cheng, Y.; Su, W.; Su, A. Optimization of heterogeneous continuous flow hydrogenation using FTIR inline analysis: a comparative study of multi-objective Bayesian optimization and kinetic modeling. *Chem Eng Sci*. 2025, 302, 120901. https://doi.org/10.1016/j.ces.2024.120901.
19. Yamashiro, H.; Nonaka, H. Estimation of processing time using machine learning and real factory data for optimization of parallel machine scheduling problem. *Oper Res Perspect*. 2021, 8, 100196. https://doi.org/10.1016/j.orp.2021.100196.
20. Cao, J.; Xia, X.; Wang, L.; Zhang, Z.; Liu, X. A Novel Multi-Efficiency Optimization Method for Disassembly Line Balancing Problem. *Sustainability*. 2019, 11, 6969. https://doi.org/10.3390/su11246969.
21. Xu, W.; Tang, Q.; Liu, J.; Liu, Z.; Pham, DC. Disassembly sequence planning using discrete Bees algorithm for human-robot collaboration in remanufacturing. *Robot Comput-Integr Manuf*. 2020, 62, 101860. https://doi.org/10.1016/j.rcim.2019.101860.
22. Chu, M.; Chen, W. Human-robot collaboration disassembly planning for end-of-life power batteries. *J Manuf Syst*. 2023, 69, 271-291. https://doi.org/10.1016/j.jmsy.2023.06.014.
23. Xing, Y.; Wu, D.; Qu, L. Parallel disassembly sequence planning using improved ant colony algorithm. *Int J Adv Manuf Technol*. 2021, 113, 2327-2342. https://doi.org/10.1007/s00170-021-06753-9.
24. Yang, Y.; Yuan, G.; Zhuang, Q.; Tian, G. Multi-objective low-carbon disassembly line balancing for agricultural machinery using MDFOA and fuzzy AHP. *J Clean Prod*. 2019, 233, 1465-1474. https://doi.org/10.1016/j.jclepro.2019.06.035.

25. Liu, H.; Zhang, L. Optimizing a disassembly sequence planning with success rates of disassembly operations via a variable neighborhood search algorithm. *IEEE Access*. 2021, 9, 157540-157549. http://dx.doi.org/10.1109/ACCESS.2021.3101221.
26. Tuo, Y.; Zhang, Z.; Wu, T.; Zeng, Y.; Zhang, Y.; Junqi, L. Multimanned disassembly line balancing optimization considering walking workers and task evaluation indicators. *J Manuf Syst*. 2024, 72, 263-286. https://doi.org/10.1016/j.jmsy.2023.11.011.
27. Li, Y.; Liu, L. Physics-Informed Neural Network-Based Nonlinear Model Predictive Control for Automated Guided Vehicle Trajectory Tracking. *World Electr Veh J*. 2024, 15, 460. https://doi.org/10.3390/wevj15100460.
28. Cruz, Y J.; Villalonga, A.; Castaño, F. Automated machine learning methodology for optimizing production processes in small and medium-sized enterprises. *Oper Res Perspect*. 2024, 12, 100308. https://doi.org/10.1016/j.orp.2024.100308.
29. Li, H.; Li, L.; Jiao, S.; Zhao, F.; Southerland, JW.; Yin, F. An improved identification method based on Bayesian regularization optimization for the imbalanced proportion plastics recycling using NIR spectroscopy. *J Mater Cycles Waste Manag*. 2024, 26, 3838-3851. https://doi.org/10.1007/s10163-024-02083-6.
30. Wang, J.; Tian, Y.; Hu, X.; Li, Y.; Zhang, K.; Liu, Y. Predictive modelling and Pareto optimization for energy efficient grinding based on aANN-embedded NSGA II algorithm. *J Clean Prod*. 2021, 327, 129479. https://doi.org/10.1016/j.jclepro.2021.129479.
31. Kroon, M. An Eulerian constitutive model for rate-dependent inelasticity enhanced by neural networks. *Comput Methods Appl Mech Eng*. 2024, 430, 117241. https://doi.org/10.1016/j.cma.2024.117241.
32. Masuda, T.; Tanabe, K. Neural network ensembles for band gap prediction. *Comput Mater Sci*. 2025, 246, 113327. https://doi.org/10.1016/j.commatsci.2024.113327.
33. Zhou, T.; Zhou, H.; Li, M.; Yan, S. A neural network method for the escape rate in metastable system. *Physica A*. 2025, 674, 130759. https://doi.org/10.1016/j.physa.2025.130759.
34. Wang, K.; Ren, J.; Yan, J.; Wu, X.; Dang, F. Research on a concrete compressive strength prediction method based on the random forest and LCSSA-improved BP neural network. *J Build Eng*. 2023, 76, 107150. https://doi.org/10.1016/j.jobe.2023.107150.
35. Chen, G.; Tang, B.; Zeng, X.; Zhou, P.; Kang, P.; Long, H. Short-term wind speed forecasting based on long short-term memory and improved BP neural network. *Int J Electr Power Energy Syst*. 2022, 134, 107365. https://doi.org/10.1016/j.ijepes.2021.107365.
36. Wang, Z.; Xie, C.; Liu, B.; Jiang, Y.; Li, Z.; Tai, H. Self-adaptive temperature and humidity compensation based on improved deep BP neural network for NO2 detection in complex environment. *Sens Actuators B Chem*. 2022, 362, 131812. https://doi.org/10.1016/j.snb.2022.131812.
37. Wu, L.; Yang, Y.; Maheshwari, M.; Li, N. Parameter optimization for FPSO design using an improved FOA and IFOA-BP neural network. *Ocean Eng*. 2019, 175, 50-61. https://doi.org/10.1016/j.oceaneng.2019.02.018.
38. Zhang, L.; Zhao, X.; Ke, Q.; Dong, W.; Zhong, Y. Disassembly line balancing optimization method for high efficiency and low carbon emission. *Int J Precis Eng Manuf-Green Technol*. 2019, 8, 233-247. https://doi.org/10.1007/s40684-019-00140-2.
39. Lee, M L.; Behdad, S.; Liang, X,; Zheng, M. Task allocation and planning for product disassembly with human–robot collaboration. *Robot Comput-Integr Manuf*. 2022, 76, 102306. https://doi.org/10.1016/j.rcim.2021.102306.
40. Hartono, N.; Ramírez, FJ.; Pham, DT. A multiobjective decision-making approach for modelling and planning economically and environmentally sustainable robotic disassembly for remanufacturing. *Comput Ind Eng*. 2023, 184, 109535. https://doi.org/10.1016/j.cie.2023.109535.
41. Xu, Z.; Han, Y. Two sided disassembly line balancing problem with rest time of works: A constraint programming model and an improved NSGA II algorithm. *Expert Syst Appl*. 2023, 239, 122323. https://doi.org/10.1016/j.eswa.2023.122323.
42. Li, Y.; Zhu, W.; Guo, J.; Wang, K.; Gao, L. Multi-objective collaborative optimization of green disassembly planning and recovery option decision considering the learning effect. *J Manuf Syst*. 2025, 80, 324-343. https://doi.org/10.1016/j.jmsy.2025.03.011.
43. Xiao, J.; Terzi, S. Large language model-guided graph convolution network reasoning system for complex human-robot collaboration disassembly operations. *Procedia CIRP*. 2025, 134, 43-48. https://creativecommons.org/licenses/by-nc-nd/4.0.
44. Yin, L.; Wang, C.; Cong, L.; Du, Q. A sequential disassembly planning approach based on knowledge graph and graph isomorphism network for supporting power battery remanufacturing. *J Clean Prod*. 2025, 507, 145558. https://doi.org/10.1016/j.jclepro.2025.145558.
45. Shin, Y.; Kim, Z.; Yu, J.; Kim, G.; Hwang, S. Development of NOx reduction system utilizing artificial neural network (ANN) and genetic algorithm (GA). *J Clean Prod*. 2019, 232, 1418-1429. https://doi.org/10.1016/j.jclepro.2019.05.276.
46. Tharwat, A.; Schenck, W. A conceptual and practical comparison of PSO-style optimization algorithms. *Expert Syst Appl*. 2021, 167, 114430. https://doi.org/10.1016/j.eswa.2020.114430.
47. Liu, R.; Liu, Y.; Jiao, L.; Wang, L. Multi-objective optimization of reservoir group operation after Inter-basin water transfer jointing SWAT model and NSGA-II. J *Hydrol*. 2025, 66, 133431. https://doi.org/10.1016/j.jhydrol.2025.133431.

48. Wang, Q.; Jia, X. Multi-objective optimization of CFRP drilling parameters with a hybrid method integrating the ANN, NSGA-II and fuzzy C-means. *Compos Struct*. 2020, 235, 111803. https://doi.org/10.1016/j.compstruct.2019.111803.
49. Hongxiang, X.; Wei, W.; Bin, S.; Iibo ,L.; Yijun, C.; Jiushuai, D.; Xin, S. Research on carbon emission accounting and carbon emission reduction path of coal preparation plant. *Miner Eng*. 2024, 217, 108955. https://doi.org/10.1016/j.mineng.2024.108955.
50. Chen, L.; Chen, C.; Wang, L.; Zeng, W.; Li, Z. Uncertainty quantification of once-through steam generator for nuclear steam supply system using latin hypercube sampling method. *Nucl Eng Technol*. 2023, 55, 2395-2406. https://doi.org/10.1016/j.net.2023.03.033.

Disclaimer/Publisher's Note: The statements, opinions and data contained in all publications are solely those of the individual author(s) and contributor(s) and not of MDPI and/or the editor(s). MDPI and/or the editor(s) disclaim responsibility for any injury to people or property resulting from any ideas, methods, instructions or products referred to in the content.